Powder Technology 274 (2015) 28–36

Contents lists available at ScienceDirect

Powder Technology

journal homepage: www.elsevier.com/locate/powtec

Numerical modeling of the cavity phenomenon and its elimination way in rectangular radial moving bed reactor

Yi-jun He [a,1], Fang-Zhi Xiao [b,1], Zheng-Hong Luo [a,b,*]

[a] Department of Chemical Engineering, School of Chemistry and Chemical Engineering, Shanghai Jiao Tong University, Shanghai 200240, PR China
[b] Department of Chemical and Biochemical Engineering, College of Chemistry and Chemical Engineering, Xiamen University, Xiamen 361005, PR China

ARTICLE INFO

Article history:
Received 8 July 2014
Received in revised form 11 December 2014
Accepted 5 January 2015
Available online 12 January 2015

Keywords:
Rectangular radial moving bed reactor
Eulerian–Eulerian two-fluid approach
Cavity
Operation condition
Trapezoidal structure

ABSTRACT

A complete three-dimensional (3D) reactor model based on the Eulerian–Eulerian two-fluid approach was developed to assist in the understanding of the cavity phenomenon in rectangular radial flow moving bed reactors (RFMBRs). The effectiveness of proposed model was firstly validated by the experimental data. The simulation results showed that the cavity phenomenon appears on the top of catalyst bed and the cavity scale increases with the increase of the superficial gas velocity. The effects of bed voidage and solid-seal height on the formation of cavity were thoroughly investigated. It was demonstrated that an appropriate high bed voidage and solid-seal height can effectively reduce the occurrence possibility of the cavity. Moreover, it was found that a trapezoidal structure is helpful to alleviate the cavity phenomenon in RFMBRs. It is thus concluded that a numerical modeling technique provides a promising approach to eliminate the unfavorable two-phase flow as well as improve the flexibility and efficiency in RFMBRs.

1. Introduction

Moving bed reactor is a kind of multiphase flow reactor, which is characterized by particle velocity between fixed bed reactor and fluidized bed reactor. Compared with fixed bed reactor, moving bed reactor improves the internal mass transfer and heat transfer in catalyst bed due to the movement of the solid phase. Compared with fluidized bed reactor, the gas–solid contact time in moving bed reactor can change in a large range, and the flow of the solid phase is close to plug flow. Therefore, nowadays, moving bed reactors are widely applied in gas–solid or liquid–solid multiphase contact process such as the desulfurization and drying process [1–3].

As a type of moving bed reactors, in annular RFMBRs, the solid particle bed moves downward under gravity in a channel between two coaxial cylinders and the gaseous reactant mixture flows radially across the bed (see Fig. 1(a)) [4]. Generally, RFMBRs can be classified into a z-flow type and a π-flow type depending on the axial directions of the flow in the annular channel and the center pipe. If the axial flow directions in the annular channel and in the center pipe are the same, it is the z-flow type; otherwise, it is the π-flow type. On the other hand, in rectangular RFMBRs, the solid particles move downward the catalyst bed, while the gas flows into the catalyst bed from upstream face, and travels radially across the bed (see Fig. 1(b)). Whatever the flow configuration of RFMBR is, compared with axial flow moving bed reactor, a RFMBR has its unique advantages such as low pressure drop, high flow capacity and continuous regeneration of catalyst particles [4,5].

Recently, RFMBRs have been widely used in continuous catalyst regeneration reforming of UOP and IFP [4–6]. Due to the fact that the flow direction of the gas phase is perpendicular to the direction of the solid phase in RFMBR, the interaction between the gas phase and the catalyst bed can directly affect the downflow of the solid phase, and large gas velocity will lead to large pressure gradient along the gas flow direction. When the pressure gradient is sufficiently large, the gas–solid drag force exerted by the gas phase will be greater than the gravity on the solid phase. Consequently, the frictional force caused by drag force could support the weight of particles near the downstream perforated wall even in the catalyst bed, which will lead to the cease of downward motion of the particles, at least in some region adjacent to the downstream wall. In such case, the catalyst bed is said to be "pinned" [7,8]. It is worth to note that part of immobile catalyst will cause maldistributions inside the reactor and consequently lead to low reactor performance. In addition, if pinning occurs, it will form "dead zone" in catalyst bed, then the catalyst will be completely coked. On the other hand, as the gas inlet velocity increases to a sufficient large value, the normal stress caused by drag force between the particles and upstream perforated wall will decrease to a low value. When the normal stress reduces to zero, the catalyst particles begin to lose contact with the upstream perforated wall. At this moment, a cavity appears between the catalyst bed and the upstream perforated wall. Since the

* Corresponding author at: Department of Chemical Engineering, School of Chemistry and Chemical Engineering, Shanghai Jiao Tong University, Shanghai 200240, PR China. Tel./fax: +86 21 54745602.
E-mail address: luozh@sjtu.edu.cn (Z.-H. Luo).
[1] Yi-jun He and Fang-Zhi Xiao have equal contribution.

http://dx.doi.org/10.1016/j.powtec.2015.01.014
0032-5910/

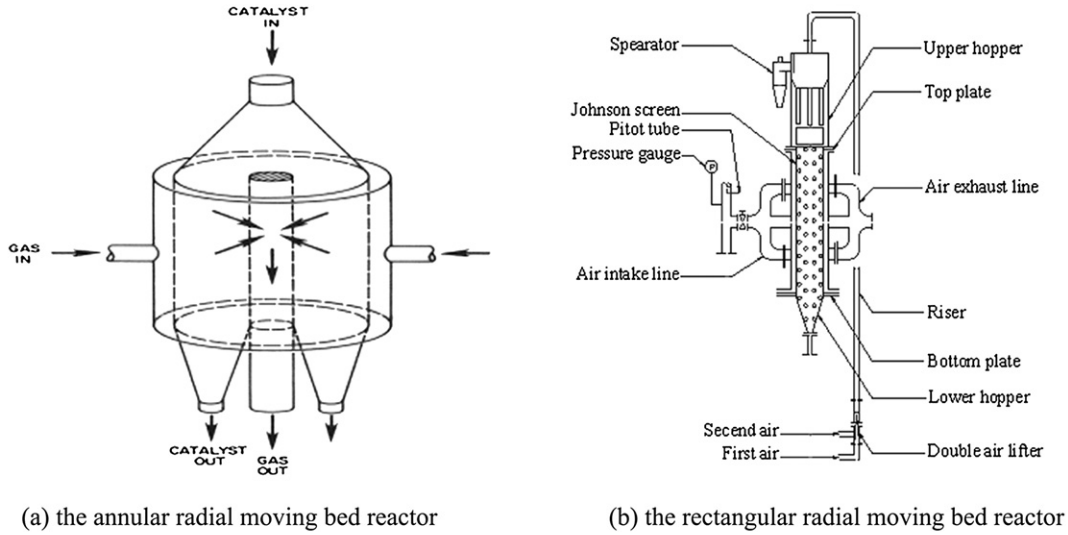

Fig. 1. The schematic diagram of annular RFMBR and rectangular RFMBR [4,5].

cavity forms in the catalyst bed, the axial distribution of gas phase becomes non-uniform or the most part of gas even flow through the cavity directly [9,10]. Moreover, some unfavorable operating factors and bad configuration in RFMBRs may lead to the inhomogeneous flow and the formations of pinning and cavity [9]. In order to operate RFMBRs more effectively and get a clear understanding of its gas–solid flow behavior, a thorough investigation of RFMBRs' hydrodynamics via numerical modeling is necessary.

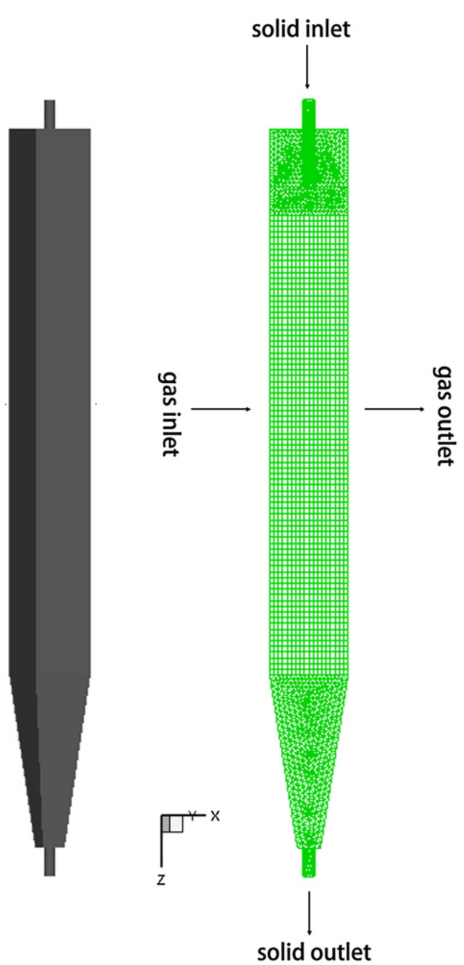

Fig. 2. The physical model and grids of 3D rectangular RFMBR.

So far, most of open reports on the RFMBR focused on the flow behavior of gas–solid two phase via theoretical or/and experimental techniques, while few on the numerical modeling of the pinning and cavity phenomenon. For instance, Ginestra and Jackson [11] performed a preliminary experimental and theoretical investigation of pinning in a system with simplified rectangular geometry. In their work, a simple analysis of the mechanics of pinning phenomenon was presented. Doyle et al. [12] developed a mathematical model to describe the pinning phenomenon in an annular moving bed reactor. Pilcher and Bridwater [13] experimentally studied the pinning phenomenon in a RFMBR. In their experiments, the cavity initiation and the partial pinning were recorded. The results demonstrated that the cavity initiation and pinning depend on the shape and the size of particles in their work [13]. Song et al. [10,14] also experimentally studied the effect of the gas flow rate on the pinning phenomenon in RFMBRs. They found that the gas flow rate is the key factor for the formation of pinning and cavity. As described above, most of the previous works mainly focused on the generation and the effects of pinning phenomenon and cavity phenomenon via experiment technique. Unfortunately, there is lack of a systematical investigation on the cavity phenomenon in RFMBRs using the experimental and modeling techniques.

In this study, we develop a complete 3D rectangular RFMBR model based on the Eulerian–Eulerian two-fluid approach to simulate the cavity phenomenon. The reactor model is validated using experimental data. Based on the validated model, both reactor operating conditions and structure are optimized to eliminate the cavity phenomenon.

2. Rectangular radial flow moving bed reactor

The experimental reactor at China University of Petroleum (Beijing) [15] was selected as the object of our simulation, which is a typical lab-scale RFMBR. The selected reactor consists of an upper hopper, a lower hopper, a catalyst bed, an entrance screen and an exit screen. The total height, width and depth of the reactor are 1900 mm,

Table 1
Parameters of particle [15].

Mean diameter/m	Particle density/kg · m^{-3}	Internal angle/°	Johnson net friction angle/°	Plexiglass friction angle/°
1.65×10^{-3}	1880	40	20.5	20

Table 2
The main governing equations [16–24].

Governing equations

1. Continuity equations of gas and solid phase

$$\frac{\partial}{\partial t}\left(\alpha_g\rho_g\right)+\nabla\cdot\left(\alpha_g\rho_g\vec{v}_g\right)=0 \tag{1}$$

$$\frac{\partial}{\partial t}(\alpha_s\rho_s)+\nabla\cdot\left(\alpha_s\rho_s\vec{v}_s\right)=0 \tag{2}$$

$$\alpha_g+\alpha_s=1 \tag{3}$$

2. Momentum equations of gas and solid phase

$$\frac{\partial}{\partial t}\left(\alpha_g\rho_g\vec{v}_g\right)+\nabla\cdot\left(\alpha_g\rho_g\vec{v}_g\cdot\vec{v}_g\right)=-\alpha_g\nabla P+\nabla\cdot\bar{\bar{\tau}}_g+K_{gs}\left(\vec{v}_s-\vec{v}_g\right)+\alpha_g\rho_g g \tag{4}$$

$$\frac{\partial}{\partial t}\left(\alpha_s\rho_s\vec{v}_s\right)+\nabla\cdot\left(\alpha_s\rho_s\vec{v}_s\cdot\vec{v}_s\right)=-\alpha_s\nabla P-\nabla P_s+\nabla\cdot\bar{\bar{\tau}}_s+K_{sg}\left(\vec{v}_g-\vec{v}_s\right)+\alpha_s\rho_s g \tag{5}$$

Where

$$\bar{\bar{\tau}}_g=\alpha_g\mu_g\left\{\left[\nabla\cdot\vec{v}_g+\left(\nabla\vec{v}_g\right)^T\right]-\frac{2}{3}\nabla\cdot\vec{v}_g{}^T\right\} \tag{6}$$

$$\bar{\bar{\tau}}_s=\alpha_s\mu_s\left[\nabla\cdot\vec{v}_s+\left(\nabla\cdot\vec{v}_s\right)^T\right]+\left(\alpha_s\lambda_s-\frac{2}{3}\alpha_s\mu_s\right)\nabla\cdot\vec{v}_s{}^T \tag{7}$$

Constitutive equations

1. Solid pressure

$$P_s=\alpha_s\rho_s\Theta_s[1+2g_0\alpha_s(1+e_s)] \tag{8}$$

2. Radial distribution function

$$g_0=\frac{1}{1-\left(\alpha_s/\alpha_{s,\max}\right)^{1/3}} \tag{9}$$

3. Solid bulk viscosity

$$\lambda_s=\frac{4}{3}\alpha_s\rho_s d_p g_0(1+e_s)\left(\frac{\Theta_s}{\pi}\right)^{1/2} \tag{10}$$

4. Solid shear viscosity

$$\mu_s=\mu_{s,col}+\mu_{s,kin}+\mu_{s,fr} \tag{11}$$

5. Collisional viscosity

$$\mu_{s,col}=\frac{4}{5}\alpha_s\rho_s d_p g_0(1+e_s)\sqrt{\frac{\Theta_s}{\pi}} \tag{12}$$

6. Kinetic viscosity

$$\mu_{s,kin}=\frac{10d_p\rho_s\sqrt{\pi\Theta_s}}{96\alpha_s(1+e_s)g_0}\left[1+\frac{4}{5}(1+e_s)\alpha_s g_0\right]^2 \tag{13}$$

7. Frictional viscosity

$$\mu_{s,fr}=\frac{P_s\ .\sin\theta}{2\sqrt{I_{2D}}} \tag{14}$$

8. Granular temperature equation

$$\frac{3}{2}\left[\frac{\partial}{\partial t}(\alpha_s\rho_s\Theta_s)+\nabla\cdot\left(\alpha_s\rho_s\vec{v}_s\Theta_s\right)\right]=\nabla\cdot\left(k_{\Theta_s}\nabla\Theta_s\right)+\left(-P_s\bar{\bar{I}}+\bar{\bar{\tau}}_s\right):\nabla\vec{v}_s-\gamma_{\Theta_s}+\phi_{gs} \tag{15}$$

Where

$$\gamma_{\Theta_s}=\frac{12\left(1-e_s^2\right)g_0}{d_p\sqrt{\pi}}\rho_s\alpha_s^2\Theta_s^{1.5} \tag{16}$$

$$\phi_{gs}=-3K_{gs}\Theta_s \tag{17}$$

9. Gas–solid drag coefficient

$$\alpha_g\le 0.8,\quad K_{sg}=150\frac{\alpha_s(1-\alpha_g)\mu_g}{\alpha_g d_p^2}+\frac{7}{4}\frac{\alpha_s\rho_g\left|\vec{v}_s-\vec{v}_g\right|}{d_p} \tag{18}$$

$$\alpha_g>0.8,\quad K_{sg}=\frac{3}{4}C_D\frac{\alpha_s\alpha_g\rho_g\left|\vec{v}_s-\vec{v}_g\right|}{d_p}\alpha_g{}^{-2.65} \tag{19}$$

$$C_D=\frac{24}{\alpha_g\mathrm{Re}_s}\left[1+\left(\frac{3}{20}\alpha_g\mathrm{Re}_s\right)^{0.687}\right] \tag{20}$$

$$\mathrm{Re}_s=\frac{\rho_g d_p\left|\vec{v}_s-\vec{v}_g\right|}{\mu_g} \tag{21}$$

10. Turbulent equations for gas phase

$$\frac{\partial}{\partial t}\left(\alpha_g\rho_g k_g\right)+\nabla\cdot\left(\alpha_g\rho_g\vec{u}_g k_g\right)=\nabla\cdot\left(\alpha_g\frac{\mu_{t,g}}{\sigma_k}\nabla k_g\right)+\left(\alpha_g G_{k,g}-\alpha_g\rho_g\varepsilon_g\right)+ K_{sg}\left(C_{sg}k_s-C_{gs}k_g\right)-K_{sg}\left(\vec{u}_s-\vec{u}_g\right)\cdot\left(\frac{\mu_{t,s}}{\alpha_s\sigma_s}\nabla\alpha_s-\frac{\mu_{t,g}}{\alpha_g\sigma_g}\nabla\alpha_g\right), \tag{22}$$

$$\frac{\partial}{\partial t}\left(\alpha_g\rho_g\varepsilon_g\right)+\nabla\cdot\left(\alpha_g\rho_g\vec{u}_g\varepsilon_g\right)=\nabla\cdot\left(\alpha_g\frac{\mu_{t,g}}{\sigma_\varepsilon}\nabla\varepsilon_g\right)+\frac{\varepsilon_g}{k_g}\left[C_{1\varepsilon}\alpha_g G_{k,g}-C_{2\varepsilon}\alpha_g\rho_g\varepsilon_g+ C_{3\varepsilon}\left(K_{sg}\left(C_{sg}k_s-C_{gs}k_g\right)-K_{sg}\left(\vec{u}_s-\vec{u}_g\right)\cdot\left(\frac{\mu_{t,s}}{\alpha_s\sigma_s}\nabla\alpha_s-\frac{\mu_{t,g}}{\alpha_g\sigma_g}\nabla\alpha_g\right)\right)\right], \tag{23}$$

11. Turbulent equations for solid phase

$$\frac{\partial}{\partial t}(\alpha_s\rho_s k_s)+\nabla\cdot\left(\alpha_s\rho_s\vec{u}_s k_s\right)=\nabla\cdot\left(\alpha_s\frac{\mu_{t,s}}{\sigma_k}\nabla k_s\right)+(\alpha_s G_{k,s}-\alpha_s\rho_s\varepsilon_s)+ K_{gs}\left(C_{gs}k_g-C_{sg}k_s\right)-K_{gs}\left(\vec{u}_g-\vec{u}_s\right)\cdot\left(\frac{\mu_{t,s}}{\alpha_s\sigma_s}\nabla\alpha_s-\frac{\mu_{t,g}}{\alpha_g\sigma_g}\nabla\alpha_g\right), \tag{24}$$

$$\frac{\partial}{\partial t}(\alpha_s\rho_s\varepsilon_s)+\nabla\cdot\left(\alpha_s\rho_s\vec{u}_s\varepsilon_s\right)=\nabla\cdot\left(\alpha_s\frac{\mu_{t,s}}{\sigma_\varepsilon}\nabla\varepsilon_s\right)+\frac{\varepsilon_s}{k_s}\left[C_{1\varepsilon}\alpha_s G_{k,s}-C_{2\varepsilon}\alpha_s\rho_s\varepsilon_s+ C_{3\varepsilon}\left(K_{gs}\left(C_{gs}k_g-C_{sg}k_s\right)-K_{gs}\left(\vec{u}_g-\vec{u}_s\right)\cdot\left(\frac{\mu_{t,s}}{\alpha_s\sigma_s}\nabla\alpha_s-\frac{\mu_{t,g}}{\alpha_g\sigma_g}\nabla\alpha_g\right)\right)\right], \tag{25}$$

Where,

$$K_{sg}\left(\vec{u}_s-\overline{u}_g\right)=K_{sg}\left(\overline{v}_s-\vec{v}_g\right)+K_{sg}\vec{v}_{dr,sg}, \tag{26}$$

$$\vec{v}_{dr,sg}=-\left(\frac{D_g}{\sigma_{sg}\alpha_s}\nabla\alpha_s-\frac{D_s}{\sigma_{sg}\alpha_g}\nabla\alpha_g\right), \tag{27}$$

$$\mu_{t,g}=\rho_g C_\mu\frac{k_g^2}{\varepsilon_g}, \tag{28}$$

$$\mu_{t,s}=\rho_s C_\mu\frac{k_s^2}{\varepsilon_s}. \tag{29}$$

Ergun resistance equations

$$\vec{S}=-\left(\frac{\mu_g}{\alpha}\vec{\nu}_g+C_2\frac{1}{2}\rho_g\left|\vec{\nu}_g\right|\vec{\nu}_g\right) \tag{30}$$

Table 2 (*continued*)

Governing equations	
Ergun resistance equations	
$\alpha = \frac{d^2}{150}\frac{\varepsilon^3}{(1-\varepsilon)^3}$	(31)
$C_2 = \frac{3.5}{d}\frac{(1-\varepsilon)}{\varepsilon^3}$	(32)

270 mm and 200 mm, respectively. The size of the upper hopper is Ø40 mm, length of 300 mm, which is buried 200 mm within the catalyst bed. The lower hopper has the length of 600 mm and its outlet tube is provided with an open valve to control the outlet velocity of particle. Besides, both sides of catalyst bed are equipped with Johnson screen with the height of 1400 mm, width of 200 mm and porosity of 16.7% (also see Fig. 2 for the reactor).

In this study, the thin packed bed is used to represent the Johnson screen and the porous media model is employed to describe the resistance offered by Johnson screen. Besides, for this rectangular RFMBR, the structured quadrilateral and hexahedral grids are applied to radial and axial directions of catalyst bed respectively. The radial and axial directions of inlet and outlet tube are meshed with triangular grid and pentahedral grid respectively. Finer cells are placed closer to the thin packed bed. In addition, the gas inlet location is set at the upstream face of catalyst bed and the gas outlet location is set at the downstream face of catalyst bed. The catalyst particles flow downward the upper hopper and depart from the outlet tube. More information regarding the rectangular RFMBR physical model and grids are shown in Fig. 2. The particle parameters are described in Table 1 [15].

3. The reactor model and solution method

In this study, a complete 3D reactor model based on the Eulerian–Eulerian two-fluid approach is developed. The Ergun resistance equations for describing the gas–solid flow behavior in the reactor are incorporated into the reactor model. The main government equations are summarized in Table 2 [16–24]. In addition, the appropriate boundary conditions and parameters are listed in Table 3. The particle size distribution is listed in Table 4 [15]. The inlet velocity is set for both the gas phase and solid phase. "Pressure outlet" boundary is used at the outlet and exit pressure is specified. At the wall, no-slip boundary conditions are set.

After initialization, the pressure, the inlet velocity and the volume fraction of particle phase in the rectangular RFMBR at initial stage are set. Before solving the equations shown in Table 2, the Ergun resistance equations are incorporated into the momentum balance equations for the gas phase as an additional momentum source term. Next, the continuity and momentum balance equations are solved. The turbulence equations are solved as well. In addition, the convergence criterion in this simulation is 1e-3, and the solution program is executed in a loop with the above solution steps until the flow time meets the given criterion. Simulations of the above coupled mode were performed with FLUENT 6.3.26 (Ansys Inc., US). A commercial grid-generation tool, GAMBIT 2.3.16 (Ansys Inc., US) was used to generate the 3D geometries and the grids. All simulations were executed in a 2.83 GHz Pentium 4 CPU with 4 GB of RAM.

Table 3
Boundary conditions and model parameters.

Description	Value
Particle–particle restitution coefficient	0.9
Gravitational acceleration ($m \cdot s^{-2}$)	9.81
Operating pressure (Pa)	1.01×10^5
Inlet boundary condition	Velocity inlet Gas inlet: 0.33 m/s Particle circulation rate: 0.3 $kg/(m^2 \cdot s)$
Outlet boundary condition	Pressure outlet
Wall boundary condition	No slip
Air density ($kg \cdot m^{-3}$)	1.255
Air viscosity ($kg \cdot m^{-3} \cdot s^{-1}$)	1.732×10^{-5}
Bed voidage	0.4

4. Results and discussion

4.1. Model validation

Herein, the simulated axial pressure gradient distribution data were compared with the experimental data [15], which is used to validate the reactor model. Fig. 3 illustrates the comparison between the simulated and experimental data with the operating conditions of superficial gas velocity of 0.33 m/s and solid-seal height of 100 mm. From Fig. 3, at the top of Johnson screen, the pressure gradient increases while decreases slightly at the bottom of it due to the end effects of Johnson screen. However, as shown in Fig. 3, the trend of simulated data using the reactor model suggested in this work is in good agreement with the experimental data [15], the maximum relative error is less than 10%. Therefore, the model used in this work can be reasonably used to simulate flow behavior in a rectangular RFMB.

4.2. The formation of cavity phenomenon

Fig. 4 shows the axial distribution contours of solid volume fraction and static pressure in rectangular RFMBR. As described in Fig. 4, the particles uniformly fill the whole reaction bed and move downward slowly like a packed bed under the action of gravity. The static pressure increases gradually along the axial direction and reaches maximum at the lower hopper due to the accumulation of particles. In addition, it decreases along the X-direction due to a high resistance offered by the solid phase, which leads to a high pressure drop. Moreover, it can be seen from Fig. 4 that the pressure drop near the upper part and the lower part of screen is lower than that in the middle of catalyst bed because of the influence of side effects, which is similar to that in experimental data [15].

Fig. 5 shows the particle velocity distribution along the catalyst bed at different radial positions. From Fig. 5, the particle velocity near the top of upstream face is higher than other positions due to the side effects. The trend of particle velocity along the axial direction of catalyst bed is almost smoothed. Besides, near the downstream face, the particle velocity is reduced slightly due to the wall friction.

Fig. 6 illustrates the axial distribution contours of solid volume fraction at different superficial gas velocities with the solid-seal height of 100 mm. As shown in Fig. 6, the catalyst particles show a complete packing state as the superficial gas velocity is no more than 0.6 m/s. When

Table 4
The particle size distribution.

Particle diameter (mm)	Mass fraction (%)
1.5–1.6	12.47
1.6–1.7	25.18
1.7–1.8	31.65
1.8–1.9	17.51
1.9–2.0	7.43
>2.0	0.72

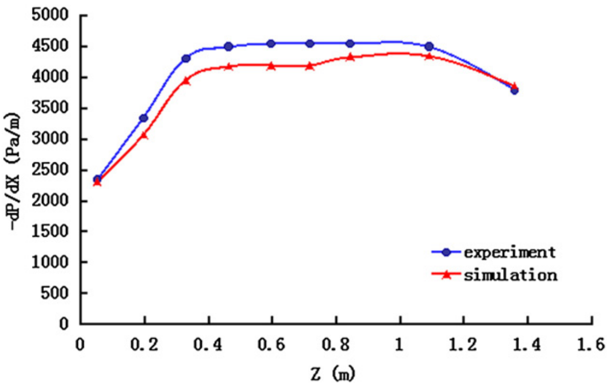

Fig. 3. Comparison of pressure gradient distribution of rectangular RFMBR between simulation and experiment. (u_{sg} = 0.33 m/s, h_{SH} = 100 mm,ε = 0.4).

the superficial gas velocity increases to 0.8 m/s, a small amount of particles begins to be fluidized and a small cavity appears at the upper part of the screen simultaneously. That can be explained by the fact that a high superficial gas velocity leads to a large pressure drop between the upstream and downstream, which would increase the gas–solid drag force and consequently decrease the normal stress between the particles and the upstream porous face. When the pressure drop increases to a critical value, the normal stress is reduced to zero and the cavity begins to form. It can be also observed from Fig. 6 that the cavity remains approximately semicircle and the cavity size increases as the superficial gas velocity increases from 0.8 m/s to 1.0 m/s. Moreover, it should be noted that once the superficial gas velocity is sufficiently large, the gas–solid drag force will prevent all particles above the cavity from moving downward. However, particles below the cavity will always move downward and consequently it would make the lower boundary of cavity move downward continuously. As a result, the shape of the cavity will change gradually from semicircle to ellipsoid.

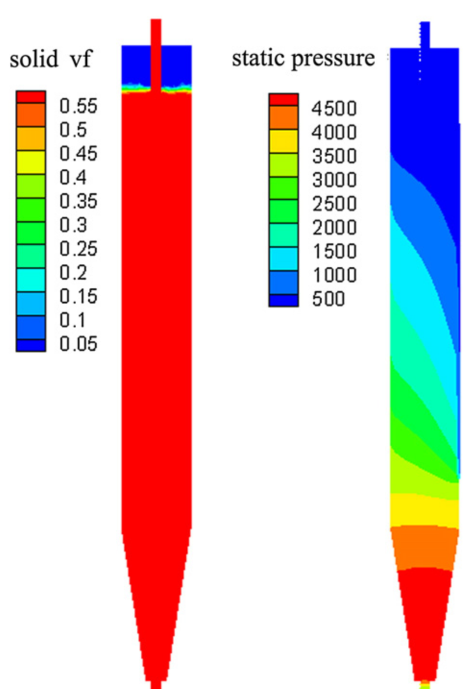

Fig. 4. The axial distribution contours of static pressure and solid volume fraction in rectangular RFMBR. (u_{sg} = 0.33 m/s, h_{SH} = 100 mm,ε = 0.4).

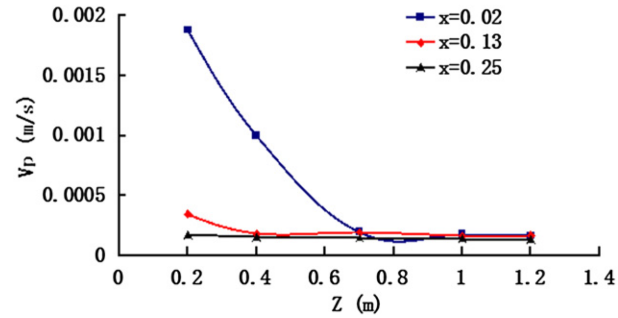

Fig. 5. The particle velocity distribution along the catalyst bed at different positions. (u_{sg} = 0.33 m/s, h_{SH} = 100 mm,ε = 0.4).

Fig. 7 shows the axial distribution of gas velocity at the superficial gas velocity of 1.0 m/s with the seal-solid height of 100 mm. It is seen from Fig. 7 that (1) the gas velocity approximately maintains a certain speed across the catalyst bed except for the cavity region; (2) the gas velocity suddenly increases at the downstream screen, which is caused by a low porosity of screen; and (3) in the cavity region, the gas flow upward near the upstream screen. Note that a high gas velocity would lead to a high pressure drop, which is in agreement with the results shown in Fig. 3. Moreover, it is implied that a relatively high superficial gas velocity of 1.0 m/s would cause the formation of cavity in the upstream screen and consequently lead to an irregular flow even short circuit in the reactor. Such an unfavorable flow field would decrease the gas–solid contact time and consequently reduces the efficiency of the reactor. How to weak or eliminate the formation of cavity has been, therefore, became an urgent wait-for-solving practical problem for meeting the requirements of industrial production, such as improvement of production capacity and reactor efficiency. In the following sections, more attentions will be paid to investigate the effects of operating conditions and reactor structure on the formation of cavity and propose the optimal control strategies for cavity elimination.

4.3. The optimization of reactor operating conditions

Based on the above discussions, it is illustrated that high superficial gas velocity plays an important role in the formation of cavity in rectangular RFMBR, which would greatly reduce the efficiency of the reactor. It is, therefore, necessary to investigate other operating conditions as well as the reactor structure to eliminate the possibility of cavity formation without the sacrifice of production capacity and operating stability of

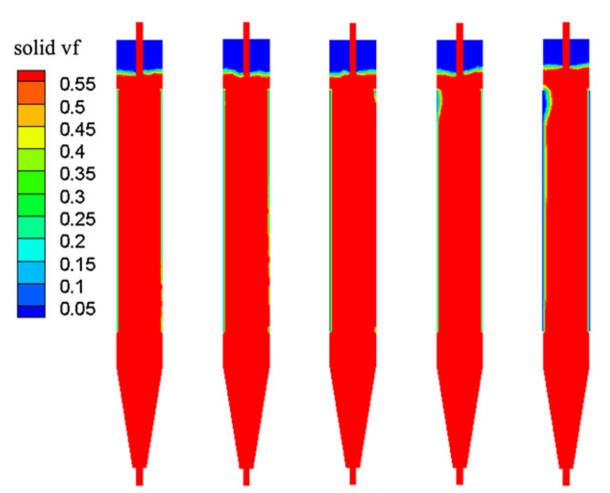

Fig. 6. The distribution contours of solid volume fraction with different superficial gas velocity under the condition of the bed voidage of 0.4. (h_{SH} = 100 mm,ε = 0.4).

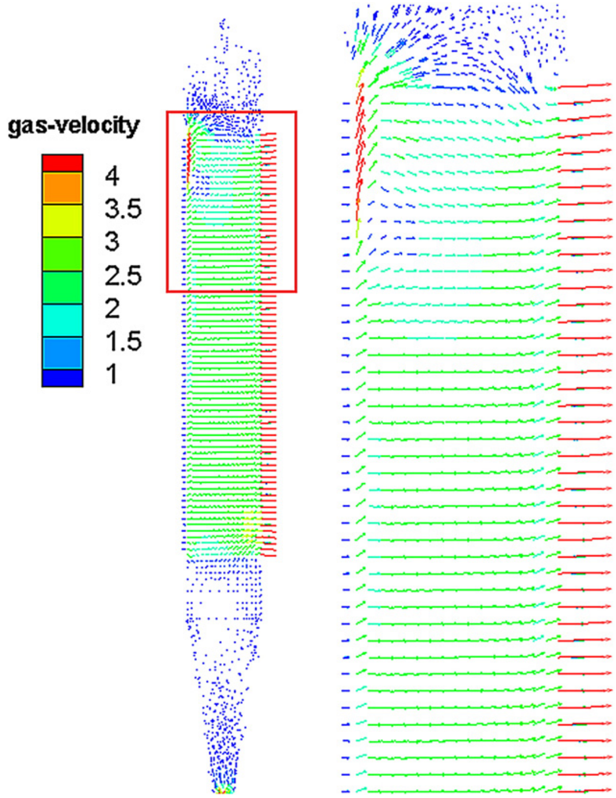

Fig. 7. The axial distribution of gas velocity with the superficial gas velocity of 1.0 m/s. (u_{sg} = 1.0 m/s, h_{SH} = 100 mm,ε = 0.4).

RFMBR. The effects of two key operating conditions, i.e., bed voidage and solid-seal height, on the cavity formation are investigated as follows.

4.3.1. Optimizing the bed voidage

Fig. 8 shows the solid volume fraction distribution contours with bed voidage of 0.5 at different superficial gas velocities. It can be observed from Fig. 8 that (1) the cavity begins to form at the left upper part of the rectangular RFMBR when the superficial gas velocity increases to 1.4 m/s; and (2) the cavity size increases with the increase of the superficial gas velocity. Compared with Fig. 6, it is found that the critical superficial gas velocity of the cavity formation increases with the increase of bed voidage. It is implied that maintaining a relatively high bed voidage is helpful to reduce the possibility of cavity formation. However, bed voidage is often determined by process requirement and needs to be appropriately adjusted in a specified range.

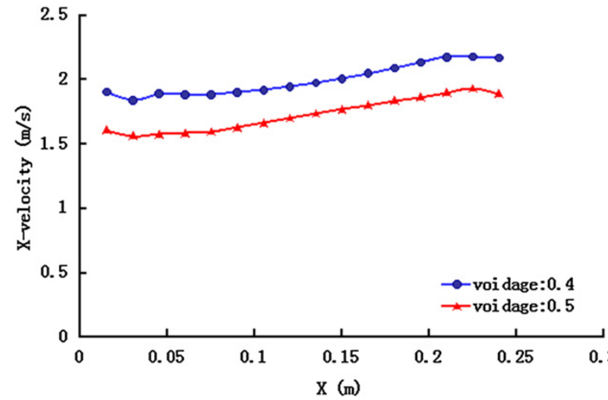

Fig. 9. The gas-x-velocity distributions along the X direction at the position of z = 1 m under the different bed voidages with the superficial gas velocity of 0.8 m/s. (u_{sg} = 0.8 m/s, h_{SH} = 100 mm).

Fig. 9 shows the gas X-velocity under the same inlet superficial gas velocity for bed voidage of 0.4 and 0.5 respectively. It is observed that gas velocity of a bed voidage of 0.5 is lower than that of a bed voidage of 0.4. That could be explained by the fact that as the bed voidage increases, the effective flow area of the whole bed will increase and consequently the gas velocity would decrease. Furthermore, as a lower gas velocity would lead to a smaller gas–solid drag force and help reduce the formation of cavity, it is thus implied that a RFMBR with a high bed voidage would help operate at relatively high gas velocity without formation of cavity, which is helpful to improve the stability and efficiency of the reactor.

4.3.2. Optimizing the bed solid-seal height

Figs. 10 and 11 illustrate the solid volume fraction distribution contours at different superficial gas velocities for solid-seal heights of 250 and 55 mm respectively. It can be seen from Figs. 6, 10 and 11 that with the decrease of the solid-seal height, the critical superficial gas velocity of the cavity formation decreases and the cavity size

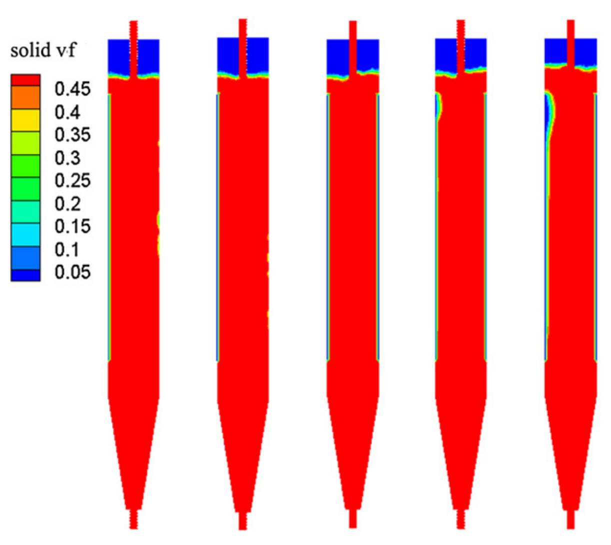

Fig. 8. The distribution contours of solid volume fraction with the different superficial gas velocity under the condition of the bed voidage of 0.5.(h_{SH} = 100 mm,ε = 0.5).

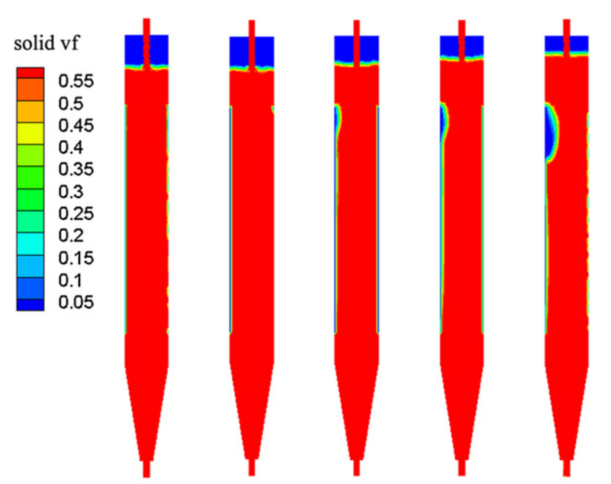

Fig. 10. The distribution contours of solid volume fraction with different superficial gas velocity under the condition of solid-seal height of 250 mm. (h_{SH} = 250 mm,ε = 0.4).

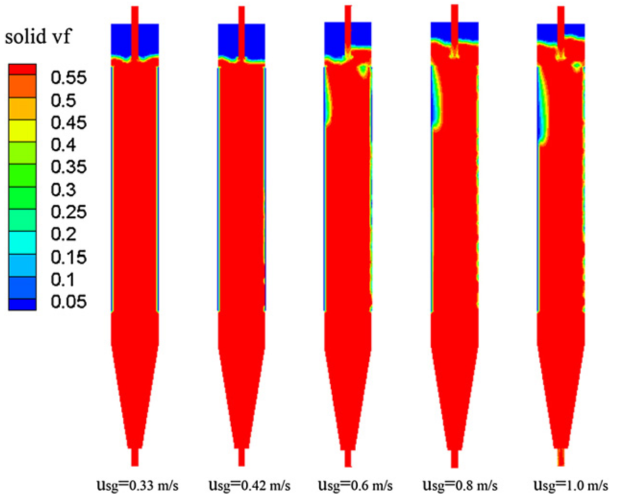

Fig. 11. The distribution contours of solid volume fraction with different superficial gas velocity under the condition of solid-seal height of 250 mm. ($h_{SH} = 55$ mm,$\varepsilon = 0.4$).

Table 5
The comparison of cavity sizes with different solid-seal heights.

Solid-seal height/mm	Superficial gas velocity/ms^{-1}	Cavity sizes/m
55	0.6	0.01
	0.8	0.032
	1.0	0.05
100	0.6	Without
	0.8	0.015
	1.0	0.032
250	0.6	Without
	0.8	Without
	1.0	0.02

increases. It is implied that increasing the solid-seal height helps increase the critical superficial gas velocity of cavity formation, which is helpful for maintaining the operating flexibility of the reactor. Meanwhile, increasing the solid-seal height would increase the pressure drop of the bed and consequently improve the circulation rate of catalyst. However, it should be noted that the occurrence possibility of unfavorable flow field in the reactor maybe increase due to the high pressure drop. Therefore, it is suggested that the solid-seal height needs to be appropriately selected at its high value based on the process requirements. Compared with Figs. 6 and 10, Fig. 11 shows a different obliquely flow structure above the Johnson screen at a relatively lower superficial gas velocity of 0.6 m/s. It is found from Fig. 11 that most of the particles above the Johnson screen move upward under the action of large drag force and accumulate on the right side of the upper hopper, where the particles almost fluidize completely. In addition, with the increase of the superficial gas velocity, the particles, near the gas inlet side, move upward gradually, which leads to an increase of the cavity size.

Table 5 shows the comparison of cavity sizes with three different solid-seal heights, i.e., 55, 100 and 250 mm. Three superficial gas velocities, i.e., 0.6, 0.8 and 1.0 m/s, are investigated for comparison. The cavity size is approximately represented as its radius. It is seen from Table 5 that (1) the critical superficial gas velocities of cavity formation are 0.6, 0.8 and 1.0 m/s for the solid-seal heights of 55, 100 and 250 mm respectively; (2) the cavity sizes at their corresponding critical superficial gas velocities are 0.01, 0.015 and 0.02 m for solid-seal heights of 55, 100 and 250 mm respectively; and (3) the cavity size decreases with the increase of solid-seal height at the same superficial gas velocity of 1.0 m/s. It is concluded that increasing solid-seal height not only helps increase the critical superficial gas velocity of cavity formation, but also reduces the cavity size.

Fig. 12 shows the development of cavity in rectangular RFMBR with the superficial gas velocity of 0.8 m/s under the condition of the solid-seal height of 55 mm. It can be observed from Fig. 12 that a small amount of gas moves upward along the cavity as cavity originating at the upper part of the catalyst bed, but the velocity decreases gradually because of the resistance of the sealing particles (see Fig. 12(a)). After a period of time, large enough gas velocity generates large drag force, which makes the sealing particles fluidized seriously. At this time, the protective effect of the solid-seal height is completely lost. The sealing particles are continuously blown and then falls. Correspondingly, a lot of the gas moves upward and swirls in the sealing hatch (see Fig. 12(b)). As a result, the unstable pressure of the catalyst bed appeared. Subsequently, the boundary of the cavity increases as the particles move downward continuously, then more particles blew to the sealing hatch and reformed a new solid-seal height (see Fig. 12(c)).

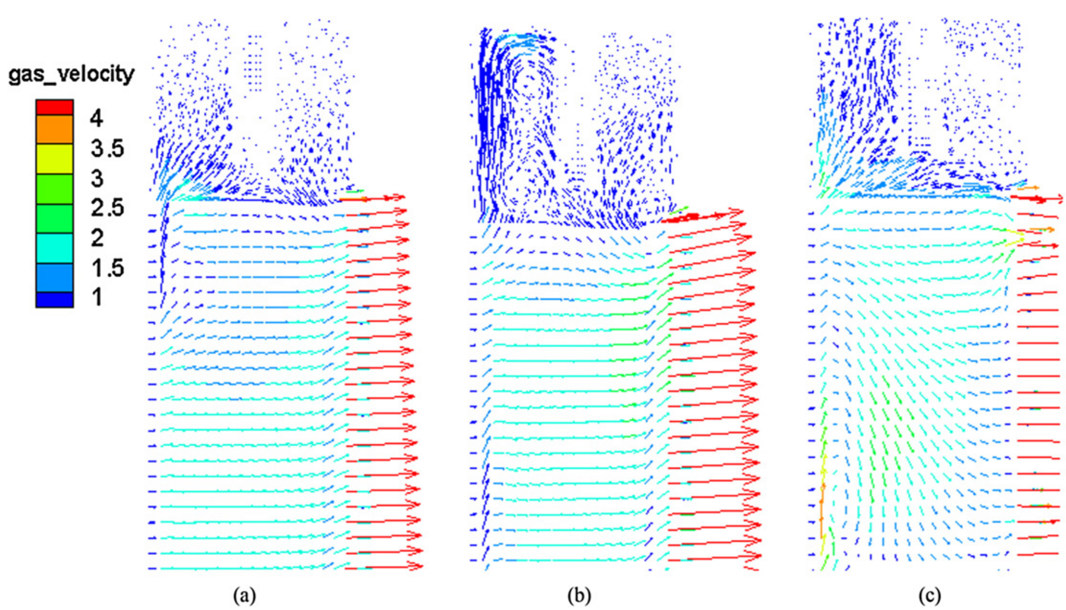

Fig. 12. The development of cavity in rectangular RFMBR under the condition of the solid-seal height of 55 mm.($u_{sg} = 0.8$ m/s, $h_{SH} = 55$ mm,$\varepsilon = 0.4$).

Thus, keeping the catalyst bed maintain a reasonable solid-seal height is meaningful for stable, safe and efficient production.

4.4. The optimization of reactor structure

The above results illustrate that with the increase of the superficial gas velocity, rectangular RFMBR is easy to generate with the cavity phenomenon on the top of the catalyst bed. It has been also demonstrated that the critical superficial gas velocity of cavity formation can be improved substantially by increasing the bed voidage and solid-seal height. In this section, an alternative strategy is investigated to further alleviate the cavity phenomenon by introducing a novel structure of RFMBR.

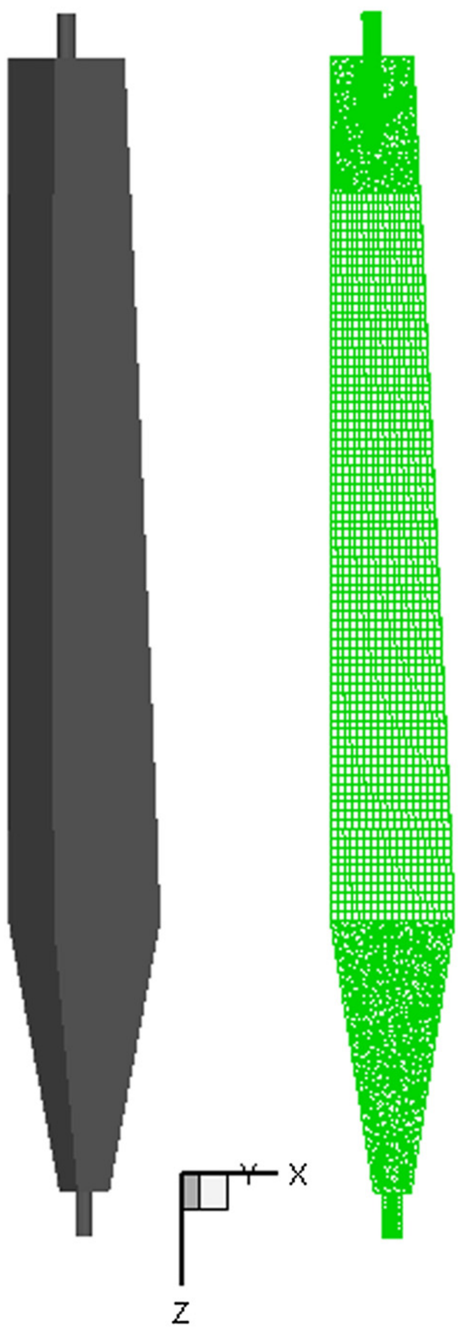

Fig. 13. The physical model and grids of 3D trapezoidal RFMBR.

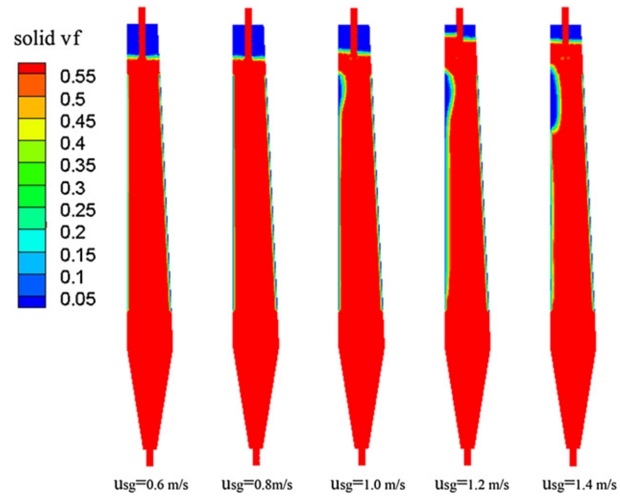

Fig. 14. The distribution contours of solid volume fraction in trapezoidal RFMBR with different superficial gas velocity. ($h_{SH} = 100$ mm,$\varepsilon = 0.4$).

In this simulation, the trapezoidal catalyst bed is used instead of the rectangular catalyst bed, where the dip angle of the downstream face is about 3°. The total height of the reactor is 1900 mm, and the widths of the upper and lower part of catalyst bed are 180 mm and 270 mm, respectively. The rest of the structure parameters is consistent with the rectangular RFMBR. More information regarding the trapezoidal RFMBR physical model and grids are provided in Fig. 13.

Fig. 14 illustrates the distribution contours of solid volume fraction in trapezoidal RFMBR at different superficial gas velocities under the conditions of solid-seal height of 100 mm and bed voidage of 0.4. It is observed from Fig. 14 that with the increase of superficial gas velocity, a cavity begins to be formed at the top of the catalyst bed and the cavity size gradually grows. It is implied that RFMBR with trapezoidal structure cannot intrinsically avoid the formation of cavity. However, compared with Figs. 6 and 14, it is found that the critical superficial gas velocity of cavity increases to 1.0 m/s when using the trapezoidal structure. Table 6 shows the comparison of cavity sizes between different structures with the superficial gas velocity of 1.0 m/s. It is found that the cavity size of 0.025 m in trapezoidal RFMBR is smaller than that of 0.032 m in rectangular RFMBR with the same superficial gas velocity. It can be explained that for trapezoidal RFMBR, smaller cross-sectional area at the top of the catalyst bed results in faster particle velocity, which can efficiently inhibit the formation of cavity. It can be concluded that adoption of trapezoidal structure in RFMBR could alleviate the formation of cavity to a certain extent. It provides a promising approach to analyze the effects of different reactor structures on cavity formation by using numerical modeling technique.

5. Conclusions

In this study, a complete 3D rectangular radial flow moving bed reactor was developed to gain a deep understanding of the hydrodynamics and cavity phenomenon of gas–solid two phase flow. The effects of catalyst bed voidage and solid-seal height on the cavity formation was thoroughly investigated. Moreover, a novel trapezoidal structure of RFMBR was studied. The main findings of the present study can be summarized as follows:

Table 6
The comparison of cavity sizes between rectangular and trapezoidal structures with the superficial gas velocity of 1.0 m/s.

Superficial gas velocity/ms^{-1}	Cavity sizes/m	
	Rectangular structure	Trapezoidal structure
1.0	0.032	0.025

(1) For rectangular RFMBR, the cavity initiates and grows gradually at the upper part of the catalyst bed with increasing the superficial gas velocity.
(2) Catalyst bed voidage and solid-seal height are two key factors to affect the formation of cavity. Increasing the bed voidage appropriately and keeping a high solid-seal height both can effectively reduce the occurrence possibility of the cavity phenomenon, ensuring the operating flexibility and stability of rectangular RFMBR.
(3) For the RFMBR, using a trapezoidal structure instead of rectangular structure is helpful to alleviate the formation of cavity phenomenon.

Nomenclature

C_D	the drag coefficient
C_2	the inertial resistant factor
C_μ, $C_{1\varepsilon}$, $C_{2\varepsilon}$, $C_{3\varepsilon}$	coefficients in turbulence model
d_p	particle diameter in catalyst bed, m
d	particle diameter in porous media, m
e_s	particle–particle restitution coefficient
G_{kg}	generation of turbulence kinetic energy due to mean velocity gradient in gas phase
g	gravitational acceleration, m/s^2
g_0	radial distribution function
$\mathrm{h_{SH}}$	solid-seal height, mm
$\bar{\bar{I}}$	identity matrix
I_{2D}	the second invariant of the deviator stress tensor
K_{gs}, K_{sg}	interphase exchange coefficient of momentum, kg/m^3 · s
k_g	turbulence kinetic energy tensor of gas phase
k_{Θ_s}	diffusion coefficient for granular energy
P	pressure, Pa
P_s	particle phase pressure, Pa
Re_s	particle Reynolds number
$R_{\varepsilon g}$	addition term in ε equation of gas phase
$\mathrm{R_r}$	the approximate radius of cavity, m
$\vec{S}$	the source term for the momentum equation
$\vec{u}_g$	gas phase weighted velocity, m/s
$\mathrm{u_{sg}}$	superficial gas velocity, m/s
$\vec{u}_s$	solid phase weighted velocity, m/s
$\vec{v}_g$	gas phase velocity, m/s
$\vec{v}_s$	solid phase velocity, m/s
α_g	volume fraction of gas phase
α_s	volume fraction of solid phase
α	permeability
γ_{Θ_s}	energy collision dissipation of energy
σ_g	turbulent Prandtl numbers for gas phase
σ_k	turbulent Prandtl numbers for k
σ_ε	turbulent Prandtl numbers for ε
ε	bed voidage
ε_g	turbulence dissipation rate of gas phase
θ	angle of internal friction, ^{0}
Θ_s	granular temperature, m^2/s^2
λ_s	solid bulk viscosity, Pa · s
μ_g	gas viscosity, Pa · s
μ_s	solid shear viscosity, Pa · s
$\mu_{l,g}$	gas molecular viscosity, (Pa · s)
$\mu_{t,g}$	the turbulent viscosity of gas phase, (Pa · s)
$\mu_{s,col}$	solid collision viscosity, Pa · s
$\mu_{s,kin}$	solid kinetic viscosity, Pa · s
$\mu_{s,fr}$	solid frictional viscosity, Pa · s
ρ_g	gas phase density, kg/m^3
ρ_s	solid phase density, kg/m^3
$\bar{\bar{\tau}}_g$	shear stress of gas phase, N/m^2
$\bar{\bar{\tau}}_s$	shear stress of solid phase, N/m^2
φ_{gs}	energy exchange between gas and solid
$\Pi_{k,g}$, $\Pi_{\varepsilon,g}$	influence of the dispersed phases on the continuous phase

Acknowledgments

The authors thank the National Ministry of Science and Technology of China (No. 2012CB21500402), the National Natural Science Foundation of China (No. U1462101) and the Research Fund for the Doctoral Program of Higher Education (No. 20130073110077) for supporting this work.

References

[1] Y.K. Ahn, H.C. Chen, T. FanL, Optimum design of a moving bed grain drier by dynamic programming, Ind. Eng. Chem. Process. Des. Dev. 3 (1964) 96–100.
[2] F.A. Zenz, D.F. Othmer, Fluidization and Fluid-Particle Systems, Reinhold, New York, 1960.
[3] B. Cha, R. Huin, H. Van Landeghem, A. Vidal, Regenerate reformers continuously, Hydrol. Processes 1 (1973) 98–101.
[4] G.J. Antos, A.M. Aitani, J.M. Parera, Catalytic Naphtha Reforming, Marcel Dekker, Inc., New York, 1995.
[5] J.H. Gary, G.E. Handwerk, Petroleum Refining, Marcel Dekker, Inc., New York, 1994.
[6] R. Gautam, P. Bogdan, J. Lichtscheidl, Maximize Use of existing assets Through advances in CCR Reforming Catalyst, European Refining Technology Conference Paris, France, 1999, pp. 23–24.
[7] J. Tsubaki, C. Tien, Solid velocity in cross flow moving beds, Powder Technol. 53 (1987) 105–112.
[8] Y.H. Chen, X.D. Zhu, Y.Q. Wu, Z.B. Zhu, Effects of internals on the particle behavior in a rectangular moving bed with gas cross-flow, Chin. J. Process Eng. 7 (2007) 639–645.
[9] Y.H. Chen, X.D. Zhu, Y.Q. Wu, Phenomenon of cavity and its size in rectangular moving-bed, J. Chem. Ind. Eng. (China) 57 (2006) 731–737.
[10] X.Q. Song, Z.W. Wang, Y. Jin, M.S. Gong, Investigations on hydrodynamics of radial flow moving bed reactors, Chem. Eng. Technol. 16 (1993) 383–388.
[11] J.C. Ginestra, R. Jackson, Pinning of a bed of particles in a vertical channel by a cross flow of gas, Ind. Eng. Fundam. 24 (1985) 121–128.
[12] F.J. Doyle, R. Jackson, J.C. Ginestra, The phenomenon of pinning in an annular moving bed reactor with crossflow of gas, Chem. Eng. Sci. 41 (1986) 1485–1495.
[13] K.A. Pinning, J. Bridgwater, Pinning in a rectangular moving bed reactor with gas cross-flow, Chem. Eng. Sci. 8 (1990) 2535–2542.
[14] X.Q. Song, Y. Jin, Z.Q. Yu, Influence of outward radial gas flow on particle movement in an annular moving bed, Powder Technol. 79 (1994) 247–256.
[15] H.H. Chen, Experiment Research of Two-phase Flow Patterns in Reforming Regenerator Radial Flow Moving Bed, China University of Petroleum (Beijing), Beijing, 1999.
[16] S. Ergun, Fluid flow through packed columns, Chem. Eng. Prog. 48 (1952) 89–94.
[17] X. Gao, Y.P. Zhu, Z.H. Luo, CFD modeling of gas flow in porous medium and catalytic coupling reaction from carbon monoxide to diethyl oxalate in fixed-bed reactors, Chem. Eng. Sci. 66 (2011) 6028–6038.
[18] C.K.K. Lun, S.B. Savage, D.J. Jeffrey, N. Chepurniy, Kinetic theories for granular flow-inelastic particles in Couette-flow and slightly inelastic particles in a general flow field, J. Fluid Mech. 140 (1984) 223–232.
[19] D. Gidaspow, Multiphase Flow and Fluidization: Continuum and Kinetic Theory Descriptions, Academic Press, Boston, 1994.
[20] J. Ding, D. Gidspow, A bubbling fluidization model using kinetic-theory of granular flow, AIChE J. 36 (1990) 523–538.
[21] B.G. Wachem, J.C. Schouten, R. Krishna, C.M.V. Bleek, J.L. Sinclair, Comparative analysis of CFD models of dense gas–solid systems, AIChE J. 6 (2001) 1035–1051.
[22] X.Z. Chen, D.P. Shi, X. Gao, Z.H. Luo, A fundamental CFD study of the gas–solid flow field in fluidized bed polymerization reactors, Powder Technol. 205 (2011) 276–288.
[23] C.J. Chen, S.Y. Jaw, Fundamentals of Turbulence Modeling, Taylor & Francis, Washington, 1998.
[24] A. Mahecha-Botero, J.R. Grace, S.S.E.H. Elnashaie, C.J. Lim, Advances in modeling of fluidized-bed catalytic reactors: a comprehensive review, Chem. Eng. Commun. 196 (2009) 1375–1405.